

Computational analysis of hydrogen flow and aerodynamic noise emission in a solenoid valve during fast-charging to fuel cell automobiles

Hifni Mukhtar Ariyadi^{a,*}, Jongsoo Jeong^b, Kiyoshi Saito^c

^a Department of Mechanical and Industrial Engineering, Faculty of Engineering, Universitas Gadjah Mada, Jl. Grafika No. 2, Yogyakarta 55283, Indonesia

^b Research Institute for Science and Engineering, Waseda University, 3-4-1 Okubo, Shinjuku-ku, Tokyo 169-8555, Japan

^c Department of Applied Mechanics and Aerospace Engineering, Waseda University, 3-4-1 Okubo, Shinjuku-ku, Tokyo 169-8555, Japan

ARTICLE INFO

Keywords:

Solenoid valve
Hydrogen
Noise
Turbulence
Computational fluid dynamics

ABSTRACT

Green energy vehicle technologies such as hydrogen-fuelled automobiles are progressing rapidly towards decarbonisation. A significant challenge in hydrogen automobiles is the storage method and safety, particularly during fast filling, including the aerodynamic noise of high-pressure systems in pressure reducer systems. In this study, a hydrogen tank solenoid (HTS) system is developed as a hydrogen supply system for fuel cell vehicles to address the above issues where one of its main parts, namely solenoid valve, works as a check valve during fast filling and as an electromagnetic pressure controller during operation. Focusing on the solenoid valve inside the HTS system, the flow characteristics and flow-induced noise during the fast charging of hydrogen are analysed via computational fluid dynamics simulation. The results show that without any treatment, the noise generated inside the solenoid valve can be extremely loud and hence adversely affect devices and users, owing primarily to severe turbulence downstream of the valve. The severe turbulence is reduced by modifying the flow path at the outlet passage, which also reduces the aerodynamic noise by 2%–12% depending on the operating conditions.

1. Introduction

Hydrogen-fuelled proton exchange membrane fuel cells (PEMFCs) have recently become popular owing to the increase in public concern and awareness pertaining to decarbonisation, which has motivated stakeholders to shift public and private vehicle power sources from hydrocarbon fuels to green energy sources. PEMFC vehicles offer many advantages compared with conventional vehicles, i.e., low operating temperature, silent operation, fast start-up, and high efficiency [11], rendering them viable as green energy vehicles.

Even though PEMFC vehicles are environmentally friendly, the safety and methodology of charging and storing fuel in the vehicles remains challenging. Although fuel charging from a gas station to a vehicle's storage tank is simple and affordable, an extremely complicated phenomenon occurs. In charging systems, the flow path of hydrogen fuel from the gas station to the vehicle's tank is extremely complex. During charging, the hydrogen pressure and temperature can increase instantly up to 70 MPa and from -40°C to 80°C, respectively, owing to the Thomson Joule effect [17].

The flow of fuel charging and discharging in hydrogen vehicles has become an interesting research topic, particularly in the field of

computational modelling involving various focuses and approaches, e.g. the thermodynamic characteristics of hydrogen fast-charging [3, 23, 26], temperature and pressure analysis of charging and discharging [12, 21, 25, 30], and dynamic simulation of charging and discharging as well as their optimisation [13, 22]. The characteristics and performance of the hydrogen flow inside different types of pressure-reducing valves for charging and discharging have been investigated, including double-stage systems [6], multistage systems [4, 5, 8, 9], Tesla valves [10], multistage Tesla valves [19], and globe valves [20].

The fast-charging process of hydrogen in PEMFC vehicles does not only imply thermal, energetic, and material issues. The flow from the station and vehicle tank during fast charging, the vehicle tank and cell stack during discharging, and the complexity of the flow path inside the charging components, such as the pressure reducing valve, involve high pressure and temperature. Consequently, complex flows, intense turbulence, and gas and wall interactions are generated, thereby resulting in energy losses, intense pressure fluctuations, and uncomfortable noise and vibrations [6]. These effects can result in mechanical failure and health and safety issues for users. Nevertheless, investigations pertaining to this issue, including approaches for minimising excessive noise and vibration, are limited. Qian et al. [19] investigated the energy losses

* Corresponding author.

E-mail address: hifni.m.a@ugm.ac.id (H.M. Ariyadi).

and sonic flow of a Tesla valve in hydrogen decompression systems to estimate the location where aerodynamic noise would most likely occur. The source of the aerodynamic noise, based on their study, is mainly energy losses from shock associated phenomena at high Mach numbers. However, they did not further investigate the aerodynamic noise generated from the systems.

Similar numerical studies pertaining to flow-induced noise in flow controllers of various gases have been published. Xu et al. [31] investigated noise generated by a control valve in underwater vehicles via a three-dimensional (3D) simulation and proposed a design improvement to reduce the noise via water injection. The valve was operated under ambient conditions with a gas flow rate of 0.11 kg/s. Wei et al. [28] used a large eddy simulation (LES) model to estimate flow-induced noise generated in a steam pressure-reducing valve at 60% opening. The steam temperature was 813 K, and the pressure ranged from 1 to 10 MPa. The design for noise reduction was improved by the addition of a perforated plate. Similarly, Yonezawa et al. [32] conducted a two-dimensional (2D) simulation of a transonic flow in a steam control valve. Semrau et al. [27] conducted experimental and theoretical studies pertaining to noise generated in a cavitating valve due to acoustic resonance. They speculated that the noise at the valves can be minimised by excluding critical operating points and modifying the system design. Yu and Yu [33] numerically and experimentally investigated the flow and sound field optimisation of an axial-flow check valve. They performed a 2D computational fluid dynamics (CFD) simulation using the standard k- ϵ model, and the design was optimised by streamlining the flow passages. The optimized design reduced the resistance coefficient and valve noise by 0.37 and 23.8 dB, respectively. Ryu et al. [24] conducted the flow and noise modelling of throttle valves and pressure reducers; they suggested that the noise can be minimised by destroying the large-scale vortex structure formed downstream.

In this study, a hydrogen tank solenoid (HTS) system was developed as a fuel supply system for hydrogen storage tanks in automobiles. The HTS system position and operative conditions during fuel charging and use are schematically shown in Fig. 1. The HTS system comprises four

main components: a filling port assembly, a solenoid valve, a manual assembly, and an inlet pipe. The gas flow during charging and usage conditions is also shown in Fig. 1. During charging, the hydrogen flows from the gas station through the HTS system from the filling port assembly to the inlet pipe before entering the storage tank, during which the fuel flows in the reverse direction to approach the fuel cell stacks.

This work aimed to reveal the aerodynamic noise generated from the hydrogen pressure controller and its sources, specifically during fast charging where the aerodynamic noise would most likely occur as it involves high intensity of complex flow phenomena. In this study, the authors focused on a solenoid pressure-reducing valve that was specifically designed for hydrogen-fueled automobiles by investigating the flow-induced noise generated during hydrogen fast charging as an initiative for design improvement and control strategies to minimise excessive noise caused by aerodynamic vibrations. The research was conducted by numerically simulating the flow via CFD simulation, where a 3D simulation was performed in two different stages. First, a steady-state simulation was performed to characterise the flow pattern and observe the sources and regions where the noise was expected to occur. Second, the simulation was continued in the transient state to investigate pressure fluctuations that result in noise by analysing the spectral data using the Ffowcs William–Hawking (FW-H) model and fast Fourier transform (FFT).

2. Numerical Model

One of the fundamental mechanisms of noise or sound generation is flow-induced noise, which occurs when pressure fluctuation is generated owing to the unsteady flow and turbulence of a fluid flow without involving any vibration of solid structures ([18] and [7]). Specifically, in pressure-reducing devices, noise is principally constructed from monopole sources due to mass flow fluctuations, dipole sources due to the solid boundary effect in the sound field, and quadrupole sources due to turbulence ([15] and [16]). The flow-induced noise can be determined and identified using a CFD approach by applying a broadband noise

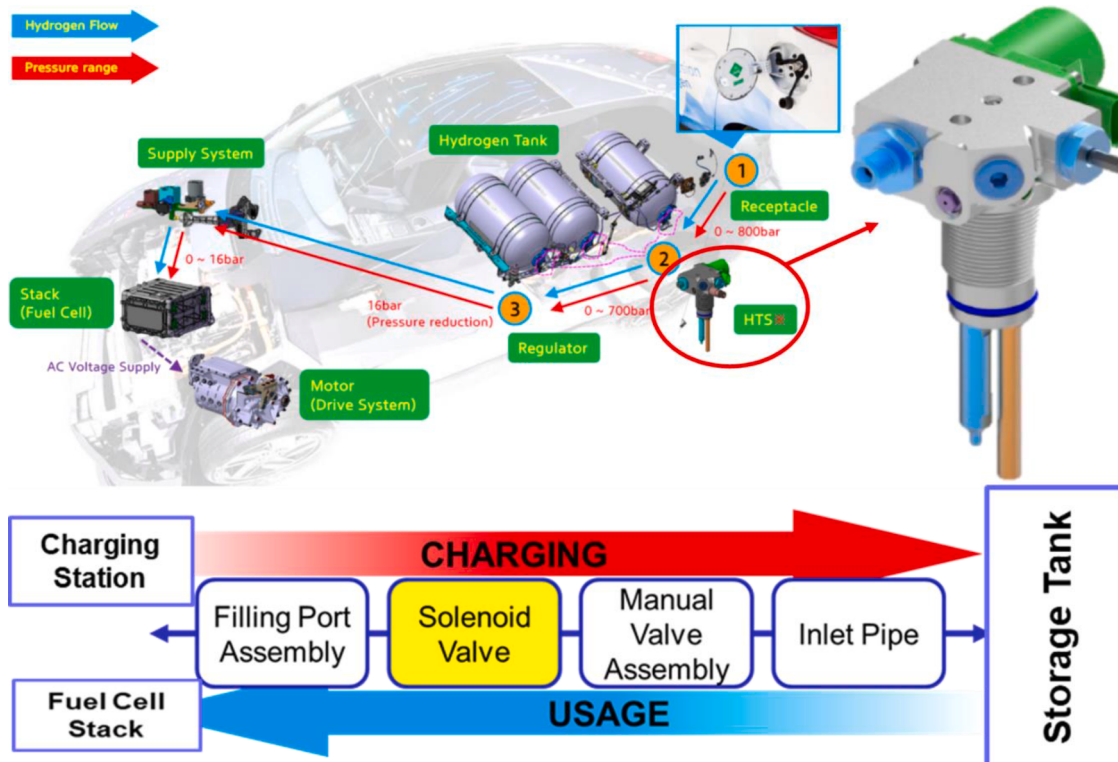


Fig. 1. Hydrogen automobile and flow path inside HTS system.

model and the FW-H model.

The mass, momentum, and energy conservation equations to be solved in the fluid flow calculation are as follows.

Mass conservation equation:

$$\frac{\partial \rho}{\partial t} + \nabla \cdot (\rho v) = 0 \quad (1)$$

Momentum conservation equation, where gravitational acceleration and external body force are disregarded:

$$\frac{\partial}{\partial t} (\rho v) + \nabla \cdot (\rho v v) = \nabla \cdot p + \nabla \cdot (\tau) \quad (2)$$

Energy conservation equation:

$$\frac{\partial}{\partial t} (\rho E) + \nabla \cdot (v(\rho E + p)) = \nabla \cdot (k_{eff} \nabla T + (\tau \cdot v)) \quad (3)$$

Here, ρ is the density (kg/m^3), v the velocity (m/s), p the static pressure (Pa), τ the viscous stress tensor, E the fluid energy (J), k_{eff} the effective conductivity, and τ_{eff} the effective stress tensor.

2.1. Broadband Noise Model

As a form of energy, the noise or sound generated from a fluid flow emits sound energy from its sources to the surrounding. The sound power generated from turbulence can be determined based on Lighthill's acoustic analogy using Eq. (4).

$$P_A = \alpha \rho_0 \left(\frac{u^3}{l} \right) \frac{u^5}{a_0^5} = \alpha_e \rho_0 \epsilon \left(\frac{\sqrt{2k}}{a_0} \right)^5, \quad (4)$$

where P_A is the sound power (W), ρ_0 the far-field density (kg/m^3), u the turbulence velocity (m/s), l the length scale (m), a_0 the speed of sound (m/s), and α and α_e are model constants; k and ϵ represent the turbulence kinetic energy per unit mass (m^2/s^2) and its dissipation rate (m^2/s^3), respectively.

The sound power level can be obtained by logarithmically scaling the acoustic power to a reference power, as shown in Eq. (5).

$$PWL = 10 \log \left(\frac{P_A}{P_{ref}} \right), \quad (5)$$

where PWL is the acoustic power level (dB), and P_{ref} is the acoustic power reference (10^{-12} W), which is the minimum sound power within the human hearing range.

By applying a broadband noise source model and identifying the turbulent intensity and vortices, the noise sources and locations can be determined.

2.2. FW-H Model

Although the broadband noise source model is used to determine the amount of sound power level emitted from a source, it does not represent the sound pressure fluctuation, which is associated with the actual audible noise generated from a flow. Therefore, a transient simulation is necessitated to capture pressure fluctuations, which correspond to "fluid vibrations" over a period. This pressure fluctuation, as the sound signal, can be computed using the FW-H model, which involves an inhomogeneous wave equation based on Lighthill's acoustic analogy; the abovementioned equation is derived from the continuity equation and Navier-Stokes equations. The FW-H equation can be expressed as shown in Eq. (6).

$$\begin{aligned} \frac{1}{a_0^2} \frac{\partial^2 p'}{\partial t^2} - \nabla^2 p' &= \frac{\partial^2}{\partial x_i \partial x_j} \{ T_{ij} H(f) \} - \frac{\partial}{\partial x_i} \{ [P_{ij} n_j + \rho u_i (u_n - v_n)] \delta(f) \} \\ &+ \frac{\partial}{\partial t} \{ [\rho_0 v_n + \rho (u_n - v_n)] \delta(f) \}, \end{aligned} \quad (6)$$

where

$$p' = p - p_0 \quad (7)$$

In Eqs. (6) and (7), p' is the sound pressure at the far-field (Pa), p the pressure (Pa), p_0 the far-field pressure (atmospheric pressure, in Pa), t the time (s), n_j the unit normal vector pointing toward the exterior region ($f > 0$), u_i the fluid velocity component in the x_i -direction (m/s), u_n the fluid velocity component normal to the source surface $f = 0$ (m/s), v_n the surface velocity component normal to the source surface $f = 0$ (m/s), T_{ij} the Lighthill stress tensor (N/m^2), $H(f)$ the Heaviside function, P_{ij} the compressive stress tensor (N/m^2), and $\delta(f)$ the Dirac delta function.

Similar to acoustic power level scaling, the sound pressure can be logarithmically scaled to a reference pressure to determine the sound pressure level (SPL), as shown in Eq. (8).

$$SPL = 10 \log \left(\frac{p'^2}{p_{ref}^2} \right), \quad (8)$$

where SPL is the acoustic pressure level (dB), and p_{ref} is the acoustic pressure reference (20×10^{-5} Pa in air), which is the minimum hearing limit of an average young human with sensitive and healthy ears, when the sound is within the frequency region of maximum hearing sensitivity [18].

The SPL data as a function of time (period) obtained using Eq. (8) was transformed into spectral data via FFT, i.e., pressure fluctuation as a function of frequency (Hz).

3. CFD Modelling

3.1. Geometry and Mesh Independency Test

The focus of this study is the pilot valve inside the solenoid valve of the HTS system, and the geometry of the fluid domain and mesh structure are illustrated in Figs. 2 (a–b). The 3D design of the fluid domain comprises three main regions: the central inlet passage, throat (pilot valve), and outlet passages. The fluid domain had a total diameter of 12.2 mm. During fast filling, the hydrogen fuel enters the central inlet passage (diameter = 3 mm) and flows dispersedly through the valve throat, which is opened depending on the pressure difference at the inlet and outlet. Once the pilot valve was passed, the fluid congregated into three identical outlets. The pilot valve is at the close and open positions when the pressure difference is zero and non-zero, respectively. When the outlet pressure, corresponds to the storage tank, is zero, the pilot valve will open at maximum opening position, allowing the hydrogen flows from the charging station to the storage tank. As the storage tank is filled with the gas, its pressure gradually increases and the pilot valve gradually closes. The hydrogen charging process, from its full opening position (0.5 mm) to fully closed position, takes around 5 minutes. The pressure and temperature gradients along the valve opening position are shown in Fig. 2 (c).

Before the simulation was conducted, a mesh dependency test was performed to determine the optimum mesh size, i.e., the largest mesh size that did not significantly affect the computation results. The mesh dependency test was performed by varying the mesh size of the fluid domain between approximately 150,000 and 4,000,000 elements for all the valve openings (i.e., 0.5, 0.3, and 0.1 mm). As a computation result parameter, the volumetric average of the sound power level was analysed, and the result indicated a deviation of less than 1% when the number of elements exceeded 1,200,000 as shown in Fig. 3. Hence, a mesh size comprising approximately 1,280,000 elements was adopted to conduct the simulation.

3.2. Simulation Method and Boundary Conditions

CFD software ANSYS Fluent v.19 [1] was used to perform the

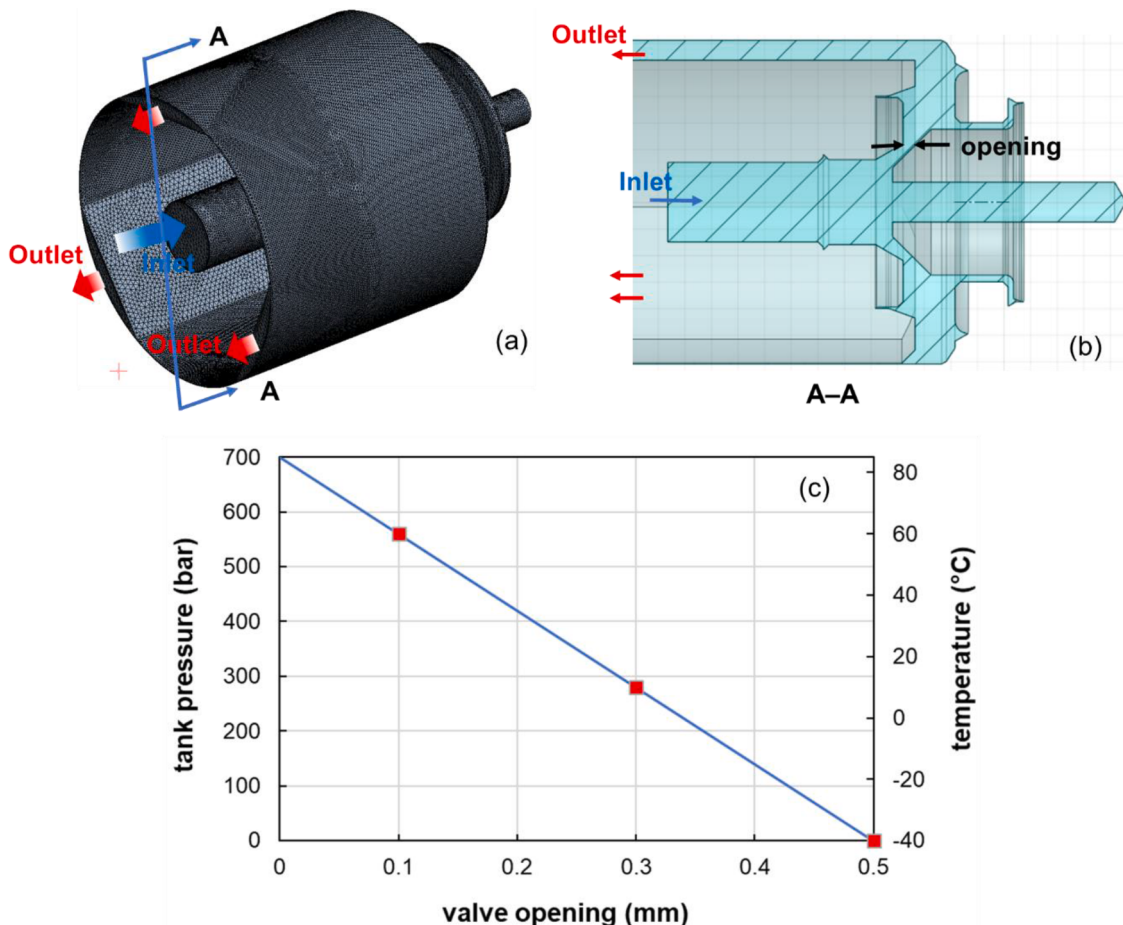


Fig. 2. Fluid domain of investigated solenoid valve: (a) 3D mesh structure and (b) half-cut view of A-A section; (c) pressure and temperature gradients along valve opening.

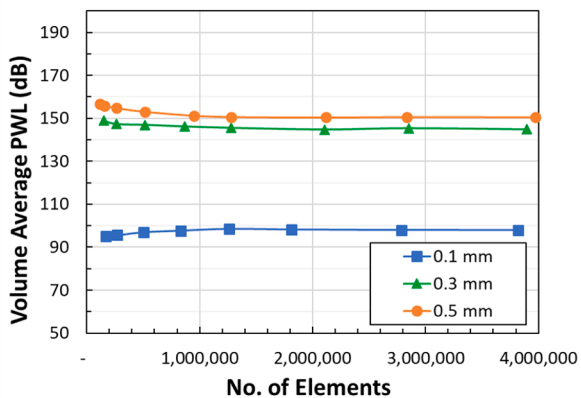


Fig. 3. Grid independency test result.

computational simulation. A steady-state simulation to characterise the hydrogen flow was performed using the realisable $k-\epsilon$ turbulence model with standard wall function. The results were used to analyse the flow pattern and determine the noise sources and locations from the turbulent intensity distribution as well as the sound power level distribution inside the valve by applying a broadband noise source model.

Subsequently, LES methods were applied in the turbulent model of the Smagorinsky–Lilly subgrid scale model and the acoustic model of the FW-H model in a transient simulation to capture the sound pressure fluctuation and actual audible noise. The time step, set as 2.5×10^{-5} s,

comprised a maximum frequency of 20,000 Hz, and the maximum iteration in each time step was set to eight. The simulation is performed on a workstation CPU with a processor of Intel(R) Xeon(R) E-2224 3.40GHz and RAM capacity of 32.0 GB. As for time cost, one transient simulation with 0.05 second of real-time can be completed within 48 hours. The pressure and velocity coupling were solved using COUPLED algorithm the pressure and momentum equations were discretized with second order and second order upwind scheme. The sound pressure at the far-field was captured by five receivers at different positions, similar to our previous study [2]. A schematic illustration of the CFD simulation workflow is shown in Fig. 4.

Two different simulation cases were investigated as the determination of the actual condition at the valve inlet is difficult. The inlet boundary condition was set at a pressure of 70 MPa for the first case, assuming the same pressure as that of the outlet gas station, and the mass flow rate was set at 30 g/s, assuming that the charging process was completed within 5 min. For this reason, with the total simulated time of 0.1 s, the valve movement during the charging process can be neglected. The outlet pressure boundary condition corresponding to the tank pressure of the vehicle was varied from 0 MPa (empty tank) to 56 MPa (almost fully charged) based on the valve opening, as shown in Table 1. Moreover, a no-slip and adiabatic wall was assumed, and the operating pressure was assumed to be 101.325 kPa. Because the charging process comprises a wide range of pressures, either constant properties of hydrogen or ideal gas approaches will result in low accuracy; therefore, real gas properties correlated from the REFPROP database library was used in the simulation [14].

To capture the sound pressure fluctuation at the far-field, five

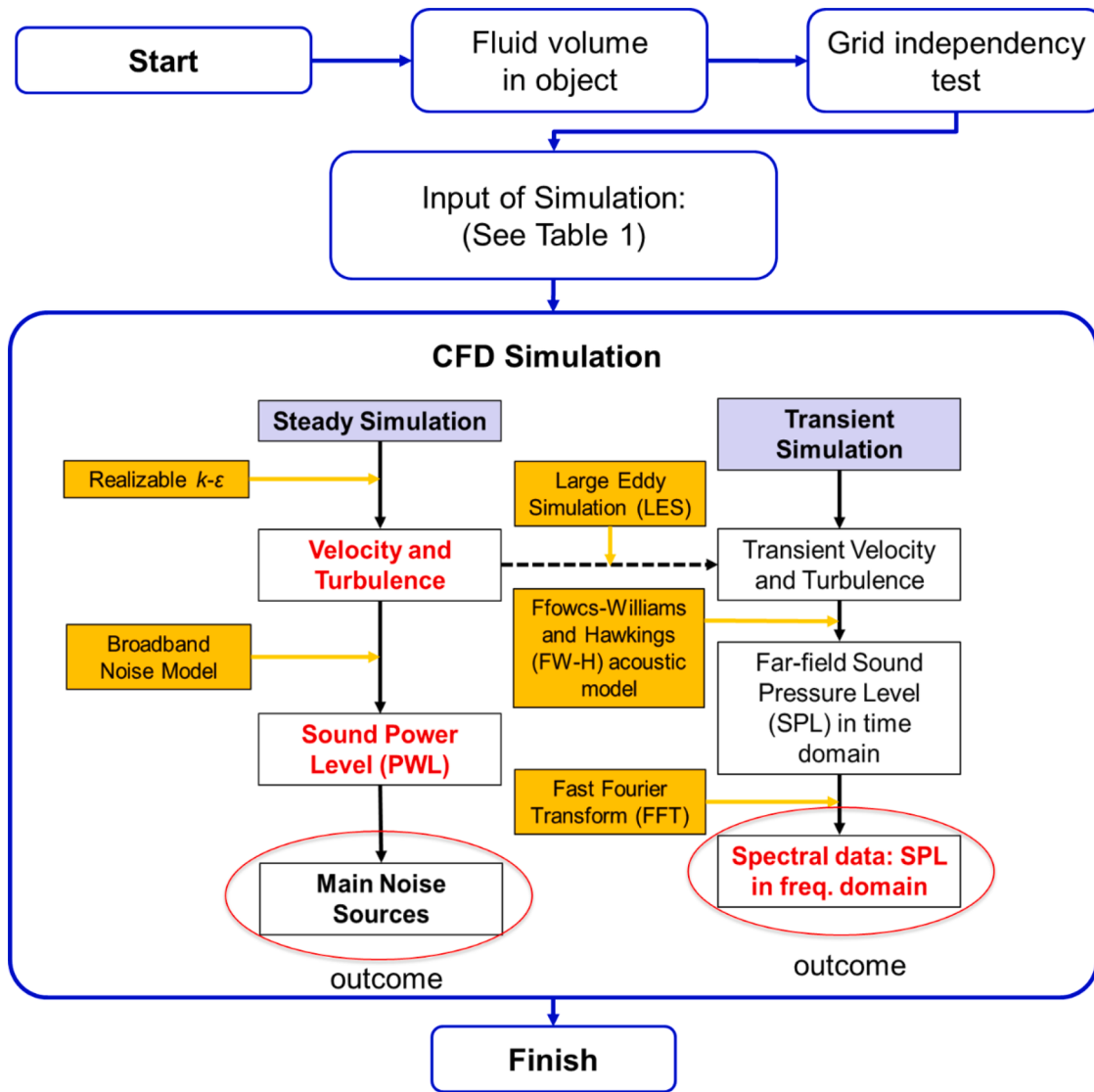


Fig. 4. CFD simulation workflow.

Table 1
Simulation operation condition.

Parameter	Value					
	Constant Pressure ($P_{in}=700$ bar)			Constant Mass Flowrate ($m_{in}=30$ g/s)		
Valve opening (mm)	0.5	0.3	0.1	0.5	0.3	0.1
m_{in} (g/s)	–	–	–	30	30	30
P_{in} (gauge bar)	700	700	700	–	–	–
P_{out} (gauge bar)	0	280	560	0	280	560
T_{in} (°C)	–40	10	60	–40	10	60

receivers were arranged at different positions at a distance of 1 m from the centre of the valve, as shown in Fig. 5. The far-field medium was atmospheric air with a pressure, density, and sound speed of 101.325 kPa, 1.225 kg/m³, and 340 m/s, respectively.

4. Results and Discussions

4.1. Fluid Flow Characteristics

4.1.1. Constant Inlet Pressure

First, the flow characteristics inside the solenoid valve are discussed

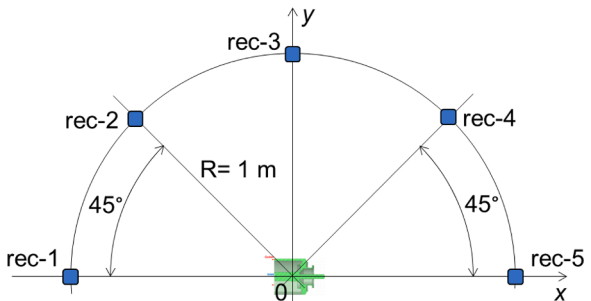


Fig. 5. Position of receivers.

prior to analysing the noise magnitudes, with emphasis primarily on velocity, turbulence, vortices, and flow separation as the main causes of flow-induced noise generation, particularly in pressure-reducing valves.

For the case of a constant inlet pressure of $P_{in} = 70$ MPa, the velocity contours for valve openings of 0.5, 0.3, and 0.1 mm are shown in Figs. 6 (a–c), respectively, on plane $z = 0$ mm. When the charging process began, the storage tank corresponded to the outlet boundary of the valve at zero pressure, and the inlet boundary experienced the charging pressure (700 bar). Consequently, the maximum pressure difference

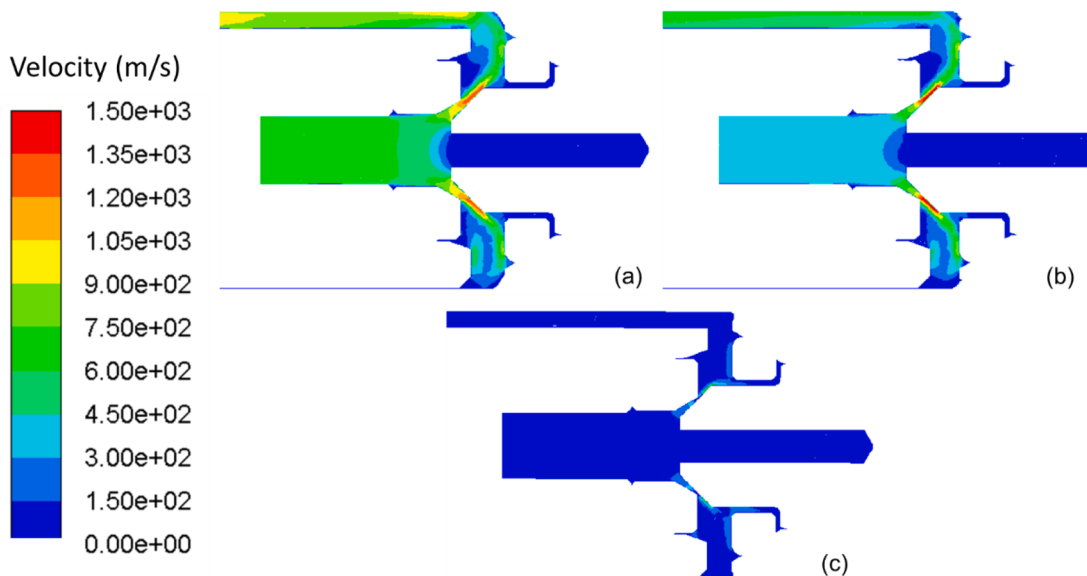


Fig. 6. Velocity contour and path line at constant pressure for openings of (a) 0.5 mm, (b) 0.3 mm, and (c) 0.1 mm.

opened the valve (0.5 mm) and generated a high hydrogen velocity. As illustrated in Fig. 6 (a), the velocity of the gas at the inlet can reach up to 627 m/s, and flow separation can be observed at the inlet region owing to obstruction and the cavity of components/wall design. The gas accelerated when entering the throat, reaching its maximum velocity and then decelerating downstream. The expanded space at the downstream and narrow three-outlet passages, in combination with several cavities of the valve components, resulted in an abrupt deceleration as well as severe vortices and turbulence.

Once charging began, the storage tank was gradually filled with the fuel, the pressure difference decreased and hence the valve opening decreased gradually; consequently, the inlet velocity decreased, as in the cases involving valve openings of 0.3 and 0.1 mm illustrated in Figs. 6 (b–c). As shown in Figs. 6 (b–c), similar flow patterns with lower magnitudes were observed, as the closing process of the valve did not significantly affect the fluid volume's geometry. Although the gas velocity downstream the valve was excessively high, it is observed that the local Mach number was still below unity. This is because the local Mach

number inside the valve corresponds to the local speed of sound in high-pressured hydrogen, that can reach as high as 1900 m/s, which is much higher than the speed of sound in air. It implies that choked flow did not occur under all conditions. Furthermore, aerodynamic noise due to jet or supersonic flow most likely did not occur. The maximum Mach number for the valve opening from 0.5 to 0.1 mm was between 0.7 and 0.9.

4.1.2. Constant Mass Flow Rate

Instead of maintaining a constant inlet pressure at the gas station pressure, the hydrogen mass flow rate was assumed to be constant at 30 g/s. Figs. 7 (a–c) depicts the velocity contours of valve openings 0.5, 0.3, and 0.1 mm, respectively, for the case involving a constant mass flow rate. As shown, the flow characteristics for this case indicated similar patterns in comparison with those of the constant pressure case. The difference is that the velocity magnitude was much smaller because the mass was assumed to be constant at 30 g/s, which is much smaller than that of the constant inlet pressure case.

When the gas charging was about to begin, the storage tank was at

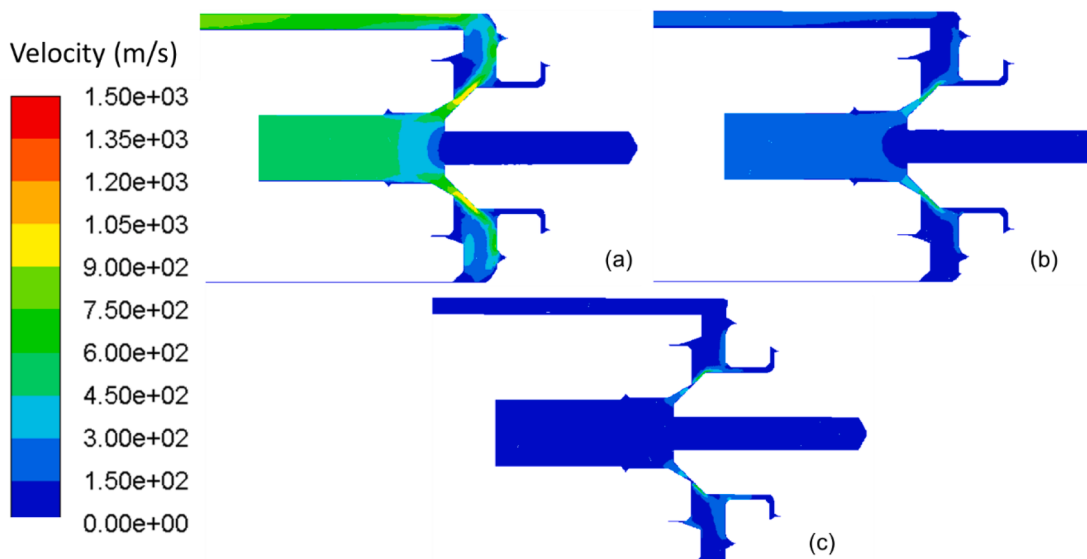


Fig. 7. Velocity contour and path line at constant mass flow rate for openings of (a) 0.5 mm, (b) 0.3 mm, and (c) 0.1 mm.

zero pressure and the valve was fully opened at 0.5 mm, allowing the gas to enter at constant mass flow rates. Owing to the low pressure in the storage tank, the specific volume of hydrogen was at its highest; consequently, the gas velocity was at its highest magnitude, as depicted in Fig. 7 (a). The simulation results show that the inlet velocity under this condition was 479 m/s.

Once the charging process started, the storage tank was pressurised with the fuel, and the valve opening began to close. As illustrated in Figs. 7 (b–c), at a pilot valve opening of 0.3 and 0.1 mm, respectively, the flow characteristics remained the same but indicated a lower velocity magnitude than that of the 0.5 mm case; this is because the higher operating pressure resulted in a lower specific volume of the fluid. The controlled mass flow rate, in addition to governing the flow pattern and velocity magnitude of the gas, indicates the absence of choked flow due to subsonic flow. Hence, aerodynamic noise due to supersonic flow most likely did not occur. In terms of the Mach number, the result shows that the maximum Mach number was from 0.8 to 0.6 for valve openings between 0.5 and 0.1 mm, and that it was observed downstream of the valve.

In addition to fluid velocity, vortices can flow separately at several locations for all valve conditions at both constant inlet pressures and constant mass flow rates, owing to the complex geometry of the valve and cavities created between the valve parts. The vortices and flow separation, which may generate noise and disturbance, occurred primarily downstream of the valve before the fluid entered the outlet passages owing to the complex structures and geometry of this region. Meanwhile, other vortices and flow separation occurred at the cylinder cave at the centre-left of the valve, thereby creating a fluid trap and hence vortices and backflows. Moreover, the unique “V and flat” in the rounded throat resulted in a collision at the flat side of the wall, a severe gas-wall interaction, and flow separation on the other side of the wall.

4.2. Noise Source and Locations

The flow characteristics of hydrogen inside a valve were revealed in the previous section. It was discovered that the flow for all operating conditions was subsonic, which implies that the shock-associated phenomena of high Mach number flow were not the main source of the noise generation. This is different to the study of Qian et al. [19] where the high Mach number in a Tesla valve of hydrogen pressure decompression system became the major source of aerodynamic noise, in addition to turbulence. In the absence of supersonic flows, the flow-induced noise

inside the pressure-reducer equipment is predominantly caused by turbulence [29]. In this study, the initial noise diagnosis was performed by identifying and localising the noise source from the turbulent intensity distribution inside the solenoid valve because the turbulence most likely affected noise generation significantly.

4.2.1. Constant Inlet Pressure

The turbulent intensity contours for the investigated zone of the valve on plane $z = 0$ mm for the case of a constant inlet pressure of 700 bar are shown in Figs. 8 (a–c). Fig. 8 (a) depicts the turbulent intensity distribution for the 0.5 mm valve opening. As shown in this figure, at the full opening condition, the velocity was the highest and subsequently, the solenoid valve emitted the highest turbulent intensity downstream of the valve. Moreover, a high turbulent intensity was detected at the flat side of the throat of the valve, caused by the gas striking the wall of the pilot valve. The backflow that occurred at the centre of the valve due to the gas trap resulted in an increase in the turbulent intensity at its entrance. In addition, a high turbulent intensity was discovered downstream, specifically in the area where the fluid was trapped and unable to reach the outlet passages, as illustrated in the figure. Consequently, an abrupt expansion and the “bottleneck” effect occurred as the fluid swirled before entering the narrow outlet passages, creating a large vortex with a high turbulent intensity. Moreover, high turbulent intensities were discovered in smaller regions where vortices and flow separation occurred, as confirmed based on the flow characteristics. At the outlet region, the turbulent intensity decreased with the vorticity, and the flow became fully developed.

The turbulent intensity contours at 0.3 and 0.1 mm valve openings are depicted in Figs. 8 (b–c), respectively. It was discovered that the solenoid valve emitted a lower turbulent intensity when the mass flow rate and fluid velocity were lower than that of the 0.5 mm valve opening. Similarly, a high turbulent intensity was detected at the surface around the entrance region, and the highest turbulent intensity was observed at the bottom side of the downstream flat side of the pilot valve throat. Beyond the downstream of the throat region, the turbulent intensity decreased significantly and became fully developed at the outlet passage.

4.2.2. Constant Mass Flow Rate

The turbulent intensity distribution for the constant mass flow case is illustrated in Figs. 9 (a–c). Because of the lower velocity, the turbulent intensity of the constant mass flow rate case was generally lower

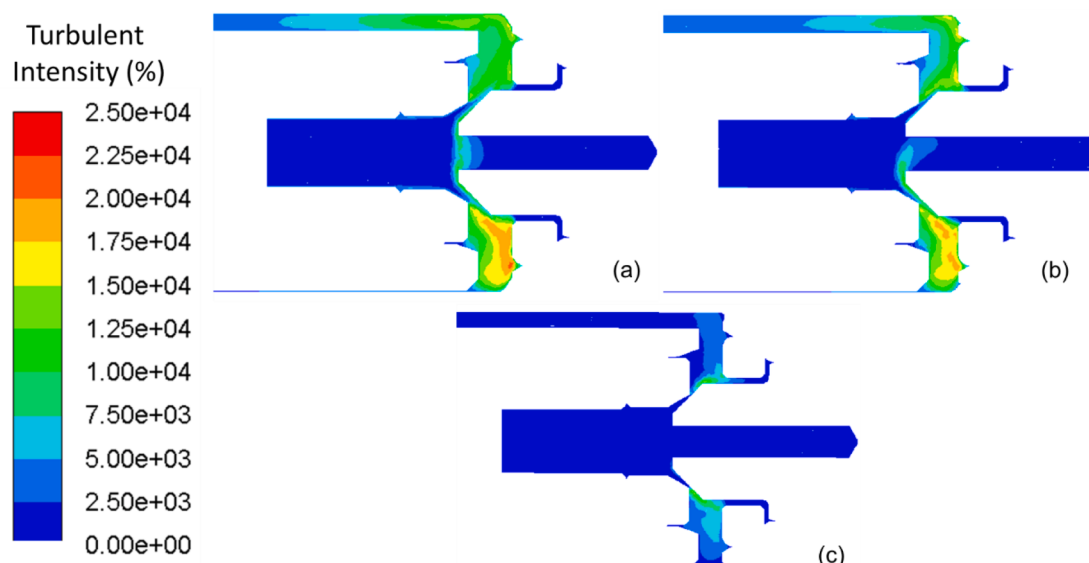


Fig. 8. Turbulent intensity contour at constant pressure for openings of (a) 0.5 mm, (b) 0.3 mm, and (c) 0.1 mm.

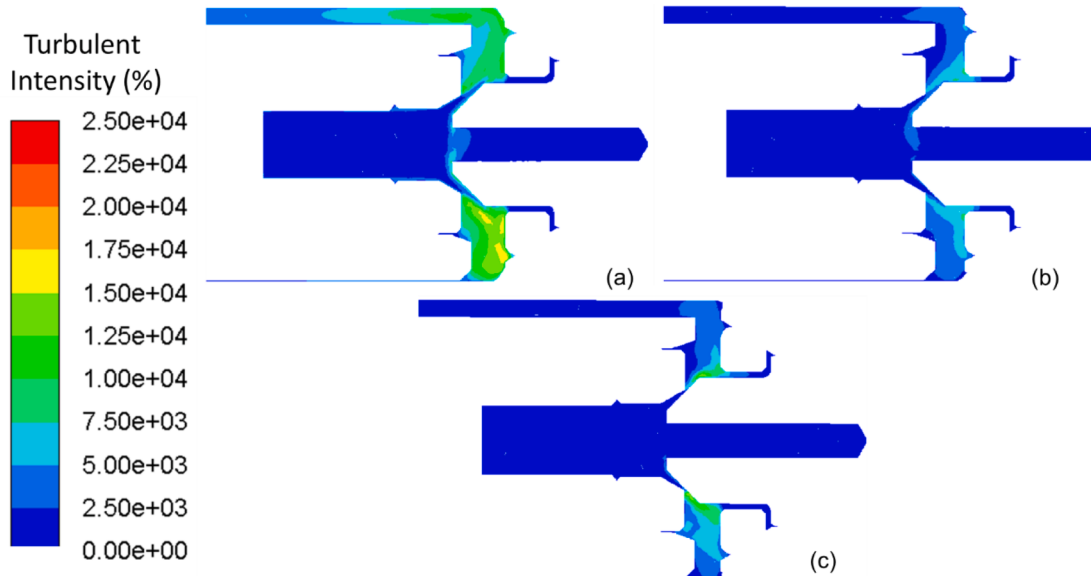


Fig. 9. Turbulent intensity contour at constant mass flow rate for openings of (a) 0.5 mm, (b) 0.3 mm, and (c) 0.1 mm.

compared with those the constant pressure case for the same valve opening.

As shown in Fig. 9 (a), which depicts the turbulence intensity contour for a 0.5 mm valve opening, the highest turbulence intensity occurred in the pilot valve, primarily downstream of the valve throat, where high velocity and vortices were discovered. Similar to the constant inlet pressure cases, a high turbulent intensity was discovered at the flat side of the throat around the entrance region, where the entering fluid hit the flat side wall of the throat. Furthermore, a high turbulent intensity was discovered at the bottom of the throat downstream, where an abrupt

expansion, the bottleneck effect, and a large vortex with an intense velocity occurred because of gas cumulation, where the gas was trapped and swirled before entering the outlet passages. Other significant turbulent intensities were detected in regions with small cavities generated by vortices and flow separation.

Figs. 9 (b–c) present the turbulent intensity distributions for the 0.3 and 0.1 mm valve opening cases, respectively. In this case, a lower turbulent intensity was discovered in the pilot valve as the mass flow rate and fluid velocity became lower than those for the 0.5 mm valve opening case. However, similar to the 0.5 mm valve opening case, areas

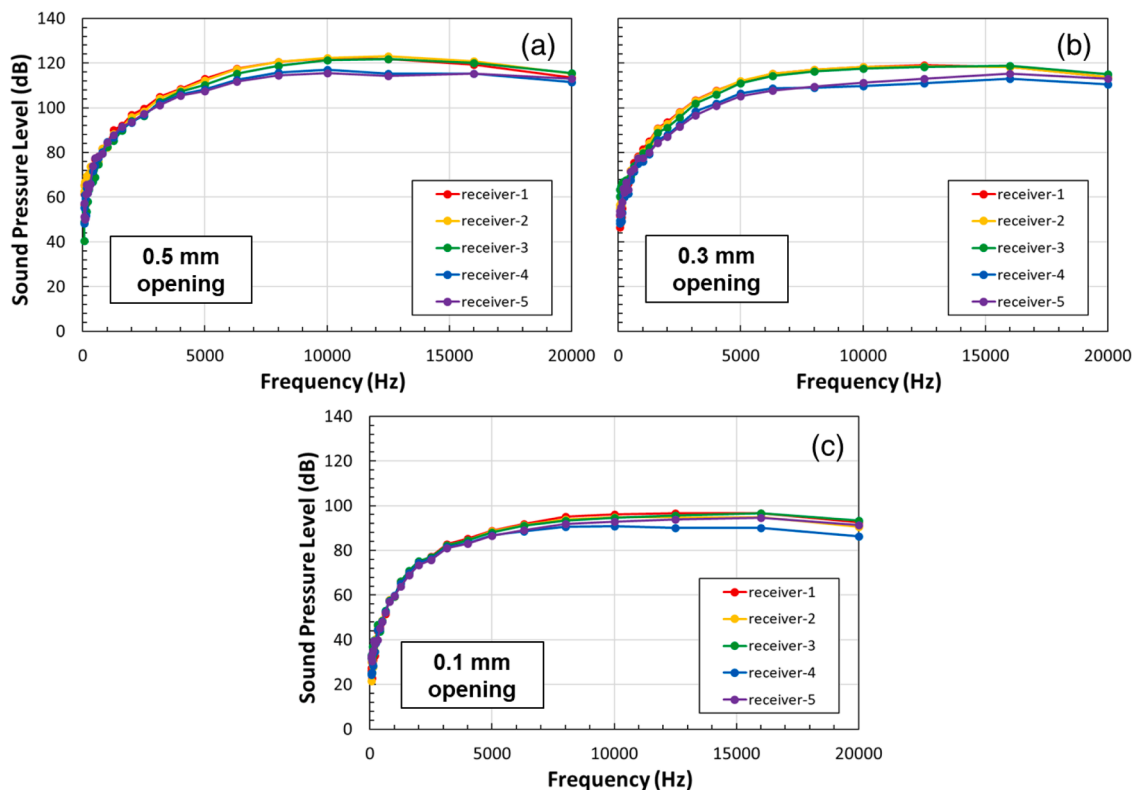


Fig. 10. Spectral data of SPL distribution around valve at constant inlet pressure for openings of (a) 0.5 mm, (b) 0.3 mm, and (c) 0.1 mm.

with a high turbulent intensity were observed at the flat side of the throat wall and the bottom side of the downstream near the wall-side of the valve. Beyond the downstream of the throat, the turbulent intensity decreased significantly, and the flow stabilised gradually at the outlet passage.

4.3. Spectral Analysis

After analysing the flow characteristics and investigating the sources of aerodynamic noise, a spectral analysis was conducted to predict audible noise by examining the *SPL* distribution in the 1/3 octave band of the frequency and the noise radiation directivity. The spectral data of the *SPL* distribution were obtained from the five receivers placed around the valves.

4.3.1. Constant Inlet Pressure

Figs. 10 (a–c) illustrate the *SPL* distribution over a frequency range of 0–20 kHz at each receiver around the valve for the constant inlet pressure case. These figures, which represent the results of the spectral data in the 1/3 octave band for 0.5, 0.3, and 0.1 mm valve openings, respectively, show similar characteristics of the *SPL* magnitude distribution over the frequency range. Because the flow at the beginning of charging exhibited the highest velocity and turbulence, the *SPL* at the 0.5 mm valve opening was generally higher than that of the 0.3 and 0.1 mm valve openings, where the flow decreased as the tank was filled. The aerodynamic noise produced by the valve was generally high at medium and high frequencies, as shown clearly for the 0.5 mm valve opening case in Fig. 10 (a), where the highest *SPL* reached 122 dB at a frequency band of 12.5 kHz. For the 0.3 mm valve opening case illustrated in Fig. 10 (b), the *SPLs* at medium and high frequencies were almost similar in magnitude, i.e. 110–120 dB. Meanwhile, for the 0.1 mm valve opening case illustrated in Fig. 10 (c), the *SPLs* at medium and high frequencies were much lower, i.e., 85–95 dB. At lower frequencies, the results show that the *SPL* magnitude decreased with the frequency for all valve opening conditions. Because the low-frequency noise was

predominantly caused by the monopole source, the noise generated inside the valve under all conditions was not pre-eminent. Furthermore, when considering the *SPL* magnitude of each receiver, all cases indicated higher *SPL* magnitudes at receivers 1, 2, and 3 than at other receivers, implying that the noise radiation in the directions of those receivers were higher.

4.3.2. Constant Mass Flow Rate

Figs. 11 (a–c) depict the results of the *SPL* distribution over a frequency range of 0–20 kHz for constant mass flow rate cases and valve openings of 0.5, 0.3, and 0.1 mm, respectively. The tendency of the *SPL* distribution shown in these figures was similar for the 0.3 and 0.1 mm valve opening cases, particularly at the medium- and high-frequency bands (higher than 6.3 kHz), and that of the 0.5 mm valve opening was similar to that of the constant inlet pressure cases. In the medium- and high-frequency bands, the *SPL* magnitudes for all valve openings were almost similar, ranging between 85 and 110 dB. For the 0.3 and 0.5 mm opening cases, the *SPL* magnitude at the high-frequency bands was slightly lower than that at the medium-frequency bands. Meanwhile, at low-frequency bands (below 6.3 kHz), the *SPL* magnitudes of the 0.5 and 0.3 mm valve openings were typically lower than those of the 0.1 mm valve opening. At the lowest band (i.e. 50 Hz), the maximum *SPLs* of the 0.5, 0.3, and 0.1 mm valve opening cases were 42, 46, and 51 dB, respectively. Although these magnitudes were not significant, the low-frequency noise that was primarily caused by the monopole source in the 0.1 mm valve opening case was likely higher than those of the 0.3 and 0.5 mm valve opening cases. The overall *SPL* in the 0.1 mm valve opening case was slightly higher than those of the 0.3 and 0.5 mm valve opening cases, although in terms of flow characteristics, the 0.1 mm opening case indicated a lower turbulent intensity. Moreover, in terms of the noise radiation direction when comparing the local *SPL* value at each receiver, all cases presented a higher *SPL* magnitude in the direction between receivers 1 and 3.

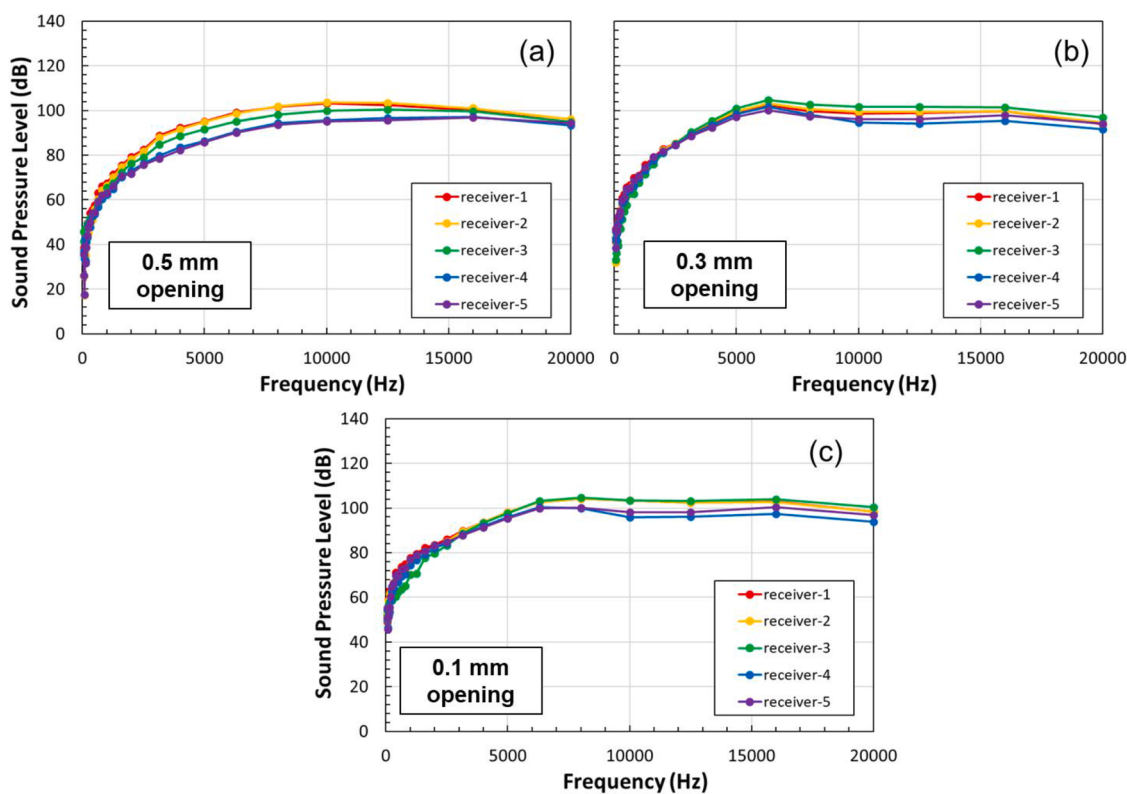


Fig. 11. Spectral data of *SPL* distribution around valve at constant mass flow rate for openings of (a) 0.5 mm, (b) 0.3 mm, and (c) 0.1 mm.

4.4. Design Improvement for Noise Reduction

The simulation results of the current solenoid valve design show that the noise generated from the induced flow was of a substantial magnitude that should be minimised to avoid any mechanical failures and health and safety issues to the users.

At this stage, modification was performed to minimise the noise generated by the fluid flow inside the solenoid valve. Considering several design constraints, such as the manufacturing process, cost, and the assembly of the valve components, only the outlet passage was considered for adjustment to reduce the turbulence downstream of the pilot valve. A combination of the reduction in the cross-sectional area and number of outlet passages are expected to increase the flow resistance and consequently reduce the velocity, turbulence, and vortex downstream of the valve, resulting in a three different proposed designs to minimize the turbulence downstream and thus the noise. In the first proposed design, the cross-sectional area of the outlet passage was reduced to 1.39 mm^2 per passage while the number of passages was kept to three passages. In the second proposed design, the cross-sectional area of the outlet passage was kept to the original area while the number of passages was reduced to two passages. The third proposed design is a combination of reduced cross-sectional area and passages. The cross-sectional view of different designs is illustrated in Fig. 12.

The simulation results of the proposed design-3 show the best in terms of the noise power source reductions, represented by the average sound power level shown in Table 2, decreased by approximately 15% for the 0.5 mm opening case but increased slightly by approximately 2% for the 0.1 mm opening case. These phenomena occurred not only in the constant pressure case ($P_{in} = 700 \text{ bar}$) but also in the constant mass flow rate case ($m_{in} = 30 \text{ g/s}$). As for the proposed design-1 and design-2, the average sound power level decreased by approximately 11% and 5%, respectively, for the 0.5 mm opening case. In the case of 0.1 mm opening, the average sound power level increased by approximately 6% and 4% for the proposed design-1 and design-2, respectively. The decrease and increase in the noise power level, however, do not represent the behaviour of actual audible noise, as represented by the SPL .

The actual audible noise reduction for the constant pressure and 0.5

mm opening cases for the three different designs is shown in Figs. 13 (a-d) where the noise generated from all proposed designs, represented in the SPL , was generally lower for all frequencies in comparison with that from the original design (Fig. 13 (a)) being the proposed design-1 show the best in noise reduction as seen in Fig. 13 (b). Whereas the maximum SPL of the original design was observed at a mid-frequency of 122 dB, the proposed design-3 indicated a maximum SPL of 105 dB. The overall SPL of the proposed design-1 was reduced by 11.1% compared with that of the original design. Although the proposed design-2 was reduced by only 1.9 %, the proposed design-3 also shows a significant amount of noise reduction, being the noise was reduced by 10.2% as depicted in Figs. 13 (c-d).

For the constant mass flow rate and 0.5 mm opening cases, the noise generated from the three proposed designs was lower than that of the original design, as shown in Table 3. The proposed design-1 indicated a maximum SPL of 89 dB, whereas the original design had a maximum SPL of 104 dB. Hence, proposed design-1 reduced the overall SPL by 12.6% in comparison with the original design. Moreover, the proposed design-2 and the proposed design-3 reduced the overall SPL by 2.5% and 8.7%, respectively, in comparison with the original design.

From the results of three different proposed designs, it can be seen that the reduction of outlet cross-sectional area gave the best of noise reduction, as demonstrated by the proposed design-1. The reason for this significant reduction was because the reduction of outlet cross-sectional area would lower the velocity of the flow without significantly increasing the vortex size downstream of the valve. In the case of proposed design-2, reducing the number of passages would lower the velocity but would also increase the vortex size downstream. Finally, reducing the cross-sectional area and number of outlet passages, as demonstrated by the proposed design-3, would reduce the aerodynamic noise but not as much as the proposed design-1 since the vortex size downstream increased as the number of passages decreased.

5. Conclusions

In this study, the flow characteristics and aerodynamic noise generated inside a solenoid valve of a hydrogen tank solenoid system

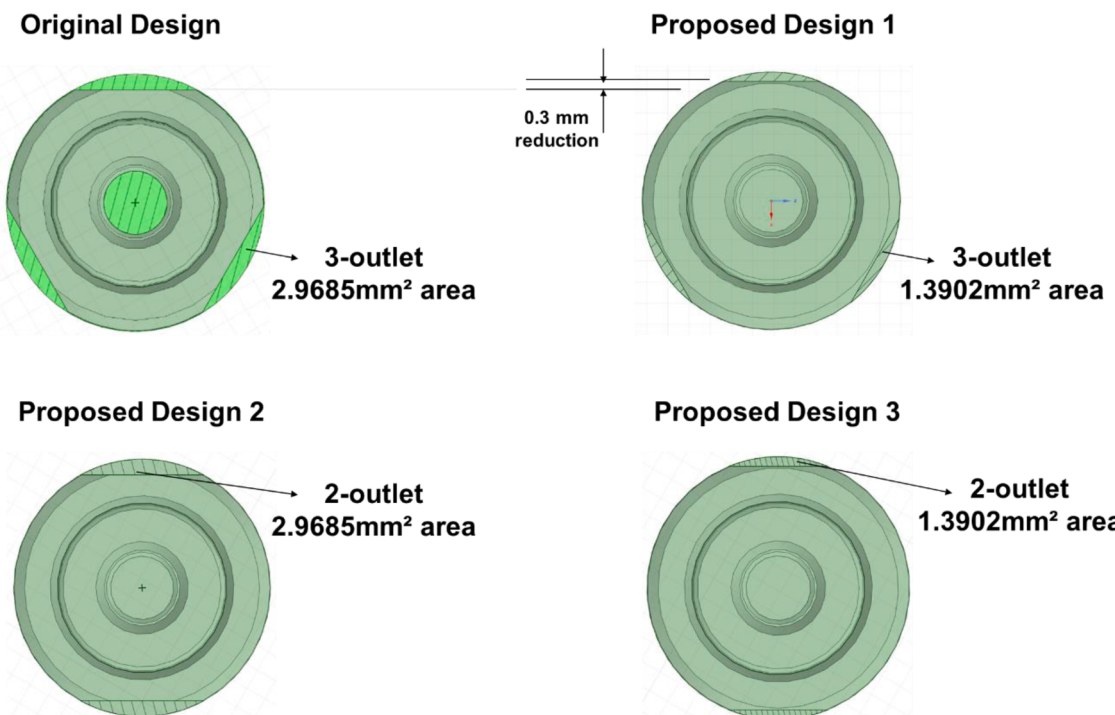


Fig. 12. Cross-sectional view of the original design and three different proposed designs.

Table 2

Average sound power level of original and proposed design.

Valve Opening (mm)	Original Design (3-outlet; normal area)			Proposed Design-1 (3-outlet; reduced area)				
	Constant $P_{in}=700$ bar	Constant $m_{in} = 30$ g/s	Avg. PWL (dB)	Constant $P_{in}=700$ bar	Constant $m_{in} = 30$ g/s	Avg. PWL (dB)		
0.5	157.4	193.6	152.8	86.4	140.3	129.3		
0.1	104.8	26.7	107.8	733.8	110.9	26.6		
Valve Opening (mm)			Proposed Design-2 (2-outlet; normal area)			Proposed Design-3 (2-outlet; reduced area)		
	Constant $P_{in}=700$ bar	Constant $m_{in} = 30$ g/s	Avg. PWL (dB)	Constant $P_{in}=700$ bar	Constant $m_{in} = 30$ g/s	Avg. PWL (dB)	Constant $P_{in}=700$ bar	Avg. PWL (dB)
0.5	151.3	163.2	145.8	106.2	134.0	92.6	128.2	203.7
0.1	108.5	31.8	107.8	683.8	107.5	29.6	107.6	702.2

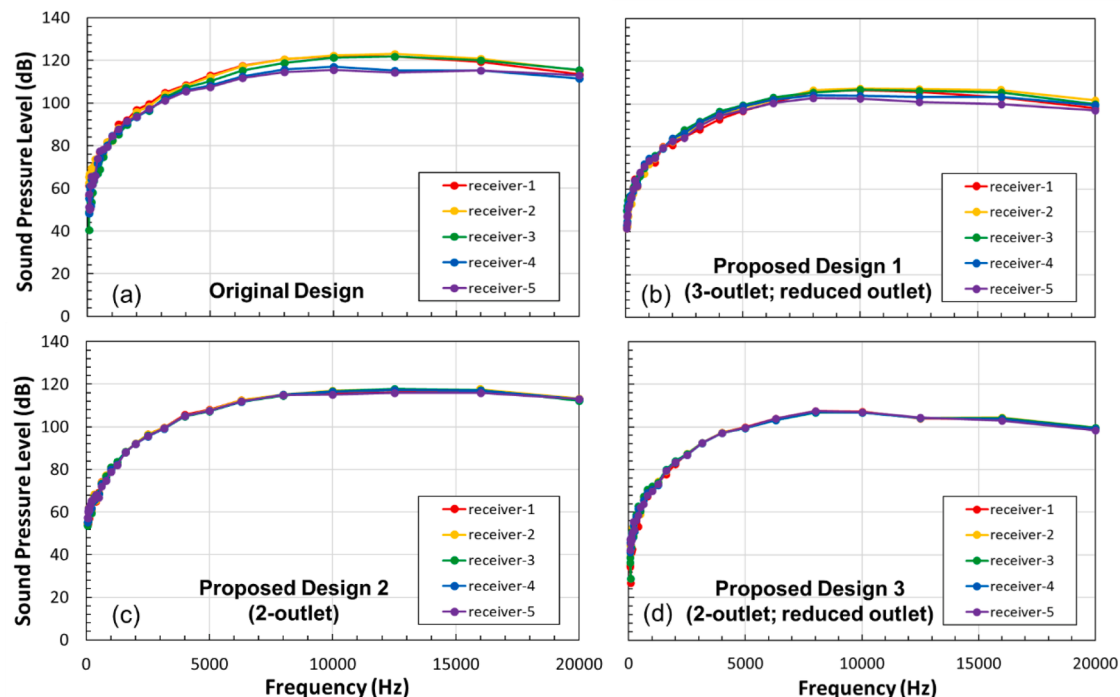
Table 3

The maximum sound pressure level of the original and proposed design at a constant mass flowrate.

Design	Maximum SPL (dB) at 0.5 mm opening and $m_{in} = 30$ g/s					% Overall noise reduction
	rec-1	rec-2	rec-3	rec-4	rec-5	
Original Design	103.1	103.8	100.5	97.2	96.9	–
Proposed Design-1	87.6	88.5	87.5	84.7	82.3	12.6
Proposed Design-2	96.9	97.5	98.0	97.8	96.4	2.5
Proposed Design-3	90.6	91.4	91.8	91.3	89.8	8.7

during the fast charging of hydrogen gas were numerically investigated using CFD simulation to address the design improvement and control strategies for decreasing unnecessary flow-induced noise. The flow analyses showed that the geometry design, which comprised several cavities, affected the generation of flow separation and vortices along the flow passages, thereby contributing as noise sources. In addition, different inlet conditions affected the local velocity and consequently resulted in turbulent intensities of various magnitudes. The highest

turbulent intensity, which is the main contributor to aerodynamic noise generation inside pressure reducer valves, was observed downstream of the throat. For all operating conditions, the flow did not reach sonic velocity, implying that aerodynamic noise from shock and sonic flow was not present in the investigated valve. In terms of audible noise prediction, the spectral data analysis showed that the *SPL* at the low-frequency bands was relatively lower than those at the medium- and high-frequency bands. Comparing the two different inlet conditions, it was evident that at a constant mass flow rate of 30 g/s, the overall *SPL* was generally lower than that of the constant inlet pressure case because the mass flow rate and velocity of the first cases were much lower than those of the latter cases. Finally, after attempting to reduce noise by modifying the outlet passage, the overall *SPL* reduced by 2%–12 %. This work provides a basis for further investigations pertaining to flow-induced noise inside a hydrogen supply system for improving design and control strategies to reduce unnecessary noise that may be unsafe to human ears. Moreover, this work can be useful for the design process of hydrogen valves of PEMFC vehicles, considering a wider perspective of safety issues as it can be also referred by researchers who are also dealing with high-pressure control systems.

**Fig. 13.** Spectral data of *SPL* distribution around valve at constant inlet pressure and 0.5 mm opening: (a) original design, (b) proposed design 1, (c) proposed design 2, and (d) proposed design 3.

CRediT authorship contribution statement

Hifni Mukhtar Ariyadi: Conceptualization, Methodology, Investigation, Visualization, Data curation, Formal analysis, Writing – original draft. **Jongsoo Jeong:** Conceptualization, Formal analysis, Supervision, Writing – review & editing. **Kiyoshi Saito:** Supervision, Writing – review & editing, Resources, Funding acquisition, Project administration.

Declaration of Competing Interest

The authors declare that they have no known competing financial interests or personal relationships that could have appeared to influence the work reported in this paper.

References

- [1] ANSYS® Academic Research CFD, Release 19.0.
- [2] H.M. Ariyadi, N. Giannetti, J. Jeong, S. Yamaguchi, K. Saito, C. Lee, J. Kim, S. Lee, J. Lee, K. Jeong, Flow characteristics and noise diagnosis of hydrogen charging solenoid valve in hydrogen-fueled automobile, in: Proceedings of the 33rd International Conference on Efficiency, Cost, Optimization, Simulation and Environmental Impact of Energy Systems, 2020, pp. 104–111.
- [3] Y. Bai, C. Zhang, H. Duan, S. Jiang, Z. Zhou, D. Grouset, M. Zhang, X. Ye, Modeling and optimal control of fast filling process of hydrogen to fuel cell vehicle, *J. Energy Storage* 35 (2021), 102306.
- [4] F. Chen, J. Qian, M. Chen, M. Zhang, L. Chen, Z. Jin, Turbulent compressible flow analysis on multi-stage high pressure reducing valve, *Flow Meas. Instrum.* 61 (2018) 26–37.
- [5] F. Chen, X. Ren, B. Hu, X. Li, C. Gu, Z. Jin, Parametric analysis on multi-stage high pressure reducing valve for hydrogen decompression, *Int. J. Hydrogen Energy* 44 (2019) 31263–31274.
- [6] F. Chen, M. Zhang, J. Qian, L. Chen, Z. Jin, Pressure analysis on two-step high pressure reducing system for hydrogen fuel cell electric vehicle, *Int. J. Hydrogen Energy* 42 (2017) 11541–11552.
- [7] M.J. Crocker, Fundamentals of acoustics, noise, and vibration, in: M.J. Crocker (Ed.), *Handbook of Noise and Vibration Control*, John Wiley & Sons, Inc, 2007, pp. 1–16.
- [8] C. Hou, J. Qian, F. Chen, W. Jiang, Z. Jin, Parametric analysis on throttling components of multi-stage high pressure reducing valve, *Appl. Therm. Eng.* 128 (2018) 1238–1248.
- [9] Z. Jin, F. Chen, J. Qian, M. Zhang, L. Chen, F. Wang, Y. Fei, Numerical analysis of flow and temperature characteristics in a high multi-stage pressure reducing valve for hydrogen refueling station, *Int. J. Hydrogen Energy* 41 (2016) 5559–5570.
- [10] Z. Jin, Z. Gao, M. Chen, J. Qian, Parametric study on Tesla valve with reverse flow for hydrogen decompression, *Int. J. Hydrogen Energy* 43 (2018) 8888–8896.
- [11] R. Krishna, E. Titus, M. Salimian, O. Okhay, S. Rajendran, A. Rajkumar, J.M. G. Sousa, A.L.C. Ferreira, J.C. Gil, J. Jose Gracio, Hydrogen storage for energy application, in: J. Liu (Ed.), *Hydrogen Storage*, IntechOpen, 2012, pp. 243–266.
- [12] T. Kuroki, N. Sakoda, K. Shiznato, M. Monde, Y. Takata, Dynamic simulation for optimal hydrogen refueling method to fuel cell vehicle tanks, *Int. J. Hydrogen Energy* 43 (2018) 5714–5721.
- [13] T. Kuroki, N. Sakoda, K. Shiznato, M. Monde, Y. Takata, Prediction of transient temperature of hydrogen flowing from pre-cooler of refueling station to inlet of vehicle tank, *Int. J. Hydrogen Energy* 43 (2018) 1846–1854.
- [14] E.W. Lemmon, I.H. Bell, M.L. Huber, M.O. McLinden, NIST Standard Reference Database 23: Reference Fluid Thermodynamic and Transport Properties-REFPROP, Version 7.0, National Institute of Standards and Technology, Standard Reference Data Program, Gaithersburg, 2004.
- [15] M.J. Lighthill, On sound generated aerodynamically I. General theory, *Proc. Royal Soc. London A* 211 (1952) 564–587.
- [16] M.J. Lighthill, On sound generated aerodynamically II. Turbulence as a source of sound, *Proc. Royal Soc. London A* 222 (1954) 1–32.
- [17] Y.L. Liu, Y.Z. Zhao, L. Zhao, X. Li, H.G. Chen, L.F. Zhang, H. Zhao, R.H. Sheng, T. Xie, D.H. Hu, J.Y. Zheng, Experimental studies on temperature rise within a hydrogen cylinder during refuelling, *Int. J. Hydrogen Energy* 35 (2010) 2627–2632.
- [18] M.P. Norton, D.G. Karczub, *Fundamentals of Noise and Vibration Analysis For Engineers*, Cambridge University Press, 2003.
- [19] J. Qian, M. Chen, Z. Gao, Z. Jin, Mach number and energy loss analysis inside multi-stage Tesla valves for hydrogen decompression, *Energy* 179 (2019) 647–654.
- [20] Qian J., Liu B., Lei L., Zhang H., Lu A., Wang J., Jin Z., Effects of orifice on pressure difference in pilot-control globe valve by experimental and numerical methods, 4 (2016) 18562–18570.
- [21] E. Rothuizen, B. Elmegård, M. Rokni, Dynamic simulation of the effect of vehicle-side pressure loss of hydrogen fueling process, *Int. J. Hydrogen Energy* 45 (2020) 9025–9038.
- [22] E. Rothuizen, W. Merida, M. Rokni, M. Wistoft-Ibsen, Optimization of hydrogen vehicle refueling via dynamic simulation, *Int. J. Hydrogen Energy* 38 (2013) 4221–4231.
- [23] E. Ruffio, D. Saury, D. Petit, Thermodynamic analysis of hydrogen tank filling. Effects of heat losses and filling rate optimization, *Int. J. Hydrogen Energy* 39 (2014) 12701–12714.
- [24] J. Ryu, C. Cheong, S. Kim, S. Lee, Computation of internal aerodynamic noise from a quick-opening throttle valve using frequency-domain acoustic analogy, *Appl. Acoust.* 66 (2005) 1278–1308.
- [25] N. Sakoda, K. Onoue, T. Kuroki, K. Shiznato, M. Kohno, M. Monde, Y. Takata, Transient temperature and pressure behavior of high-pressure 100MPa hydrogen during discharge through orifices, *Int. J. Hydrogen Energy* 41 (2016) 17169–17174.
- [26] S. Schafer, H. Klein, Thermodynamical analysis of a hydrogen fueling station via dynamic simulation, *Int. J. Hydrogen Energy* 44 (2019) 18240–18254.
- [27] S. Semrau, R. Skoda, W. Wustmann, K. Habr, Experimental and numerical investigation of noise generation due to acoustic resonance in a cavitating valve, *J. Sound Vib.* 463 (2019), 114956.
- [28] L. Wei, G. Zhu, J. Qian, Y. Fei, Z. Jin, Numerical simulation of flow-induced noise in high pressure reducing valve, *PLoS ONE* 10 (6) (2015), e0129050.
- [29] L. Wei, G. Zhu, Y. Fei, L. Chen, Z. Jin, The effects of orifice plate on the aerodynamic noise in high pressure reducing valve, *Proc. Mtgs. Acoust.* 20 (2013), 040001.
- [30] J. Xiao, J. Cheng, X. Wang, P. Benard, R. Chahine, Final hydrogen temperature and mass estimated from refueling parameters, *Int. J. Hydrogen Energy* 43 (2018) 22409–22418.
- [31] W. Xu, Q. Wang, D. Wu, Q. Li, Simulation and design improvement of a low noise control valve in autonomous underwater vehicles, *Appl. Acoust.* 146 (2019) 23–30.
- [32] K. Yonezawa, R. Ogawa, K. Ogi, T. Takino, Y. Tsujimoto, T. Endo, K. Tezuka, R. Morita, F. Inada, Flow-induced vibration of a steam control valve, *J. Fluids Struct.* 35 (2012) 76–88.
- [33] J. Yu, S. Yu, Numerical and experimental research of flow and sound fields in an axial-flow check valve and its optimization, *Adv. Mech. Eng.* 7 (11) (2015) 1–8.